Monthly Notices
of the
ROYAL ASTRONOMICAL SOCIETY

MNRAS **512,** 2389–2401 (2022)
Advance Access publication 2022 February 28

https://doi.org/10.1093/mnras/stac545

The evolution of the Si IV content in the Universe from the epoch of reionization to cosmic noon

V. D'Odorico [1,2,3]★ K. Finlator [4,5,12] S. Cristiani,[1,3] G. Cupani [1,3] S. Perrotta,[6] F. Calura [7] M. Cènturion,[1] G. Becker [8] T. A. M. Berg [9,10] S. Lopez [10] S. Ellison [11] and E. Pomante[1]

[1]*INAF - Osservatorio Astronomico di Trieste, Via Tiepolo 11, I-34143 Trieste, Italy*
[2]*Scuola Normale Superiore di Pisa, Piazza dei Cavalieri 7, I-56126 Pisa, Italy*
[3]*IFPU - Institute for Fundamental Physics of the Universe, via Beirut 2, I-34151 Trieste, Italy*
[4]*Department of Astronomy, New Mexico State University, Las Cruces, NM 88003, USA*
[5]*Cosmic Dawn Center (DAWN), Niels Bohr Institute, University of Copenhagen/DTU-Space, Technical University of Denmark*
[6]*Department of Astronomy, University of California, San Diego, CA 92092, USA*
[7]*INAF - Osservatorio Astronomico di Bologna, Via Ranzani 1, I-40127 Bologna, Italy*
[8]*Department of Physics & Astronomy, University of California, Riverside, CA 92521, USA*
[9]*ESO - European Southern Observatory, Alonso de Cordova 3107, Casilla 19001, Santiago, Chile*
[10]*Departamento de Astronomía, Universidad de Chile, Casilla 36-D, Santiago, Chile*
[11]*Department of Physics & Astronomy, University of Victoria, Finnerty Road, Victoria, British Columbia V8P 1A1, Canada*
[12]*Cosmic Dawn Center (DAWN), Niels Bohr Institute, University of CØpenhagen, 2100 CØpenhagen, Denmark DTU-Space, Technical University of Denmark, 2100 CØpenhagen, Denmark*

Accepted 2022 February 24. Received 2022 February 2; in original form 2021 August 20

ABSTRACT

We investigate the abundance and distribution of metals in the high-redshift intergalactic medium and circum-galactic medium through the analysis of a sample of almost 600 Si IV absorption lines detected in high- and intermediate-resolution spectra of 147 quasars. The evolution of the number density of Si IV lines, the column density distribution function, and the cosmic mass density are studied in the redshift interval $1.7 \lesssim z \lesssim 6.2$ and for $\log N(\mathrm{Si\,IV}) \geq 12.5$. All quantities show a rapid increase between $z \sim 6$ and $z \lesssim 5$ and then an almost constant behaviour to $z \sim 2$ in very good agreement with what is already observed for C IV absorption lines. The present results are challenging for numerical simulations: When simulations reproduce our Si IV results, they tend to underpredict the properties of C IV, and when the properties of C IV are reproduced, the number of strong Si IV lines [$\log N(\mathrm{Si\,IV}) > 14$] is overpredicted.

Key words: *(cosmology:)* dark ages, reionization, first stars – cosmology: observations – galaxies: high-redshift – *(galaxies:)* intergalactic medium – *(galaxies:)* quasars: absorption lines.

1 INTRODUCTION

Galaxies evolve through continuous exchanges of gas with the surrounding circum-galactic medium (CGM) and intergalactic medium (IGM). In the scenario suggested by state-of-the-art simulations, galaxies at the cosmic noon ($z \sim 2$–3) accrete a substantial fraction of their gas through 'cold flows', dense filamentary accretion streams that flow nearly unaffected through the galaxy halo and provide cold, $T \sim 10^4$ K, gas accretion to the interstellar medium (e.g. Birnboim & Dekel 2003; Kereš et al. 2005; Faucher-Giguère, Kereš & Ma 2011; van de Voort et al. 2011; Nelson et al. 2013; Theuns 2021). At the same time, the vigorous star-formation activity going on in these high-z galaxies favours the dispersion in the CGM (and eventually, IGM) of the metal-enriched gas through feedback mechanisms driven by galactic winds, Super Nova (SN) explosions, and accretion on to black holes (e.g. Madau, Ferrara & Rees 2001; Calura & Matteucci 2006; Barai et al. 2013; Suresh et al. 2015; Turner et al. 2016; Muratov et al. 2017; Fossati et al. 2021).

While the observational evidence of inflowing cold flows is still tentative (e.g. Rubin et al. 2012), the presence of metal-enriched gas outside galaxies has been well established observationally for more than two decades (e.g. Cowie et al. 1995; Tytler et al. 1995; Ellison et al. 2000; Schaye et al. 2003; D'Odorico et al. 2016).

The physical properties and chemical composition of the diffuse gas are probed by absorption-line spectroscopy of bright background sources. In particular, metal absorption lines associated with H I Lyman α (Ly α) clouds with column densities $\log N(\mathrm{H\,I}) \lesssim 17.3$ are thought to arise in gas located on the outskirts of galaxies and further away, in the shallow IGM, as the H I column density decreases (van de Voort et al. 2012).

Several studies have investigated the properties of metals close to galaxies by considering the correlation between the metal absorptions observed along a quasar line of sight and the galaxies present in the field at matching redshifts. All the studies carried out up to now both at high (e.g. Adelberger et al. 2005; Steidel et al. 2010; Turner et al. 2014; Rudie et al. 2019; Lofthouse et al. 2020) and low redshift (e.g. Prochaska et al 2011; Tumlinson et al. 2011; Bordoloi et al. 2014; Liang & Chen 2014; Werk et al. 2014; Johnson et al. 2017; Fossati et al. 2019) agree on the significant presence of metals in high- and low-ionization state at impact parameters at least as large as ≈100–

★ E-mail: valentina.dodorico@inaf.it

300 kpc. The standard way to carry out this kind of investigation has been by considering samples of galaxy-absorber pairs and deducing the metal distribution in the CGM from a statistical point of view. With the advent of the 30–40 m class telescopes [e.g. the European Southern Observatory (ESO) Extremely Large Telescope],[1] it will be possible to use much fainter sources as background targets for spectroscopy (in particular, galaxies themselves) and pierce the gas surrounding the same galaxy with multiple, close lines of sight to carry out a tomographic study of the CGM. The few examples available today reveal the power of this technique to assess the gas patchiness and its covering factor around individual systems (e.g. López et al. 2018, 2020).

The distribution of metals and the enrichment mechanism at high redshift can be investigated also with large samples of absorption lines detected along many, independent lines of sight to bright sources. The statistical properties derived from those samples can then be compared with model predictions to constrain in particular the adopted feedback mechanisms (e.g. Tescari et al. 2011). The most studied ionic transition at high redshift is the triply ionized carbon doublet (C IV λλ 1548, 1551 Å) mainly due to the fact that: (i) it is commonly observed; (ii) it falls outside the Ly α forest; (iii) it is easy to identify thanks to its doublet nature; and (iv) it is observable with ground-based telescopes from $z \simeq 1.0$ to the highest redshift at which we can observe quasars to date. C IV traces ionized gas mostly in the CGM and IGM environment (see e.g. Oppenheimer & Davé 2006; Cen & Chisari 2011; Mongardi et al. 2018). The C IV number density, column density distribution function (CDDF), and cosmic mass density, $\Omega_{\rm CIV}$, are the statistical indicators mostly used to assess the evolution of the abundance of this ion across the history of the Universe (e.g. Scannapieco et al. 2006; Ryan-Weber et al. 2009; Cooksey et al. 2010; D'Odorico et al. 2010; Simcoe et al. 2011; Cooksey et al. 2013; D'Odorico et al. 2013; Codoreanu et al. 2018; Cooper et al. 2019; Meyer et al. 2019; Hasan et al. 2020). Cosmological hydrodynamical simulations by several groups have tried to reproduce the measured observables (mainly the CDDF and the cosmic mass density) all with poor results, in particular for $z \gtrsim 5$ (e.g. Keating et al. 2016; Rahmati et al. 2016, hereafter R16). The introduction of a fluctuating ultraviolet background (UVB) improves the agreement but does not solve the problem (Finlator et al. 2018, and references therein). On the other hand, Garcìa et al. (2017, hereafter G17) are able to reproduce the CDDF of C IV at $z \geq 4.35$, but at the price of an overproduction of Si IV. This overabundance of high-column density Si IV absorbers is not present in R16 and Finlator et al. (2018).

There are clear numerical limitations in the realization of the optimal C IV simulation: It should both reproduce enough strong absorbers (need of a large box) and a self-consistent, inhomogeneous UVB, implementing radiative transfer (computationally very expensive). In addition to the uncertainties in stellar yields and feedback mechanisms, the amount of C IV is made even more difficult to determine by the fact that the ionization potentials to convert C III into C IV and C IV into C V are on the opposite sides of the UVB jump due to the ionization of He II, at 4 Ryd or 54.4 eV. The shape of the UVB at energies >4 Ryd is very uncertain (see e.g. fig. 9 in Finlator et al. 2018).

Another tracer of the ionized diffuse gas in the CGM is the triply ionized silicon (Si IV λλ 1394, 1403 Å, see e.g. Steidel et al. 2010; Turner et al. 2014; Mongardi et al. 2018), which is not as common as C IV but it shares with the latter the advantage of being a doublet that is observable outside the Ly α forest. Si IV is probably tracing slightly denser gas with respect to C IV, and thus possibly closer to galaxies (e.g. Mongardi et al. 2018). However, among the absorption lines routinely detected in quasar spectra (e.g. C IV, Si IV, O VI, Mg II, and Fe II) it is the one that arises from gas in a range of densities and temperatures almost equivalent to those of gas traced by C IV (see e.g. fig. 12 in Scannapieco et al. 2006). C IV and Si IV are the dominant ionization stages of carbon and silicon in the IGM, and furthermore they are tracers of Fe-coproduction and α-element processes, respectively. Si IV can be observed from the ground for $z \gtrsim 1.15$. A bonus of Si IV with respect to C IV is that the ionization potentials to turn Si III into Si IV and Si IV into Si V fall in the energy range $2 < IP < 4$ Ryd, where the different UVB models behave very similarly.

In her pioneering work, Songaila (2001) analysed both C IV and Si IV absorption lines for a sample of 32 quasars observed with the High Resolution Spectrograph (HIRES) and the Echellette Spectrograph and Imager (ESI) at the *Keck* telescope, covering the redshift range $1.7 \lesssim z \lesssim 5.3$. Considering Si IV lines with column density $12.00 \leq \log N(\text{Si IV}) \leq 14.8$, she found that the cosmic mass density of this ion, $\Omega_{\rm SiIV}$, keeps approximately constant at lower redshift with a downturn at $z > 4.5$ (see Fig. 5). Subsequent works that investigated the properties of Si IV absorbers were all based on smaller samples and/or narrower redshift ranges (e.g. Scannapieco et al. 2006; Cooksey et al. 2011; Shull, Danforth & Tilton 2014; Boksenberg & Sargent 2015, hereafter BS15; Codoreanu et al. 2018). In general, they all confirmed the redshift behaviour of $\Omega_{\rm SiIV}$ observed by Songaila (2001). Observationally, Si IV broadly matches the behaviour of C IV in terms of redshift evolution of the cosmic mass density and line number density (e.g. Songaila 2001; BS15). Also the clustering properties of Si IV absorption lines along the line of sight are in very good agreement with those of C IV suggesting similar sizes for the ion enriched bubbles (Scannapieco et al. 2006).

For all the reasons explained above and because of the large number of available quasar lines of sight observed at intermediate to high resolution and good signal-to-noise ratio (SNR), we believe it is timely to dedicate a paper to Si IV and its statistical properties. In this work, we present a sample of 519 Si IV absorption lines with column density $\log N(\text{Si IV}) \geq 12.5$ observed along 147 quasar lines of sight and covering a very broad redshift range, $z \simeq 1.75$–6.24. Our aim is to study in detail the evolution of this ion, contrasted it with C IV and the recently studied O I (Becker et al. 2019), and provide solid observational results to be compared with simulation predictions to help figuring out the physics of the feedback mechanisms. The detailed study of the Si IV and C IV absorptions arising in the same systems (e.g. the determination and analysis of the redshift evolution of the Si IV/C IV ratio) will be deferred to a future work.

The paper is organized as follows. Section 2 describes the three spectroscopic samples that have been used in this work. In Section 3, we report the results for the line number density and CDDF computed with our sample. Section 4 is devoted to the presentation of the results on the cosmic mass density and its evolution with redshift. In section 5, we compare our results with previous works appeared in the literature. Finally, Section 6 is dedicated to the discussion and conclusions. Throughout this paper, we assume $\Omega_{\rm m} = 0.3$, $\Omega_\Lambda = 0.7$, and $h \equiv H_0/(100\ \text{km s}^{-1}\ \text{Mpc}^{-1}) = 0.70$ if not stated otherwise.

2 DATA SAMPLES AND ANALYSIS

This work is based on three samples of quasar spectra, for a total of 147 lines of sight, which cover different redshift ranges for Si IV absorptions. They are briefly described in the following sections.

In all the considered spectra, Si IV doublets were looked for by eye in the region outside the Ly α forest, redward of the quasar Ly α emission. In case of doubtful detections (e.g. blending of one of the two components of the doublet), we used the presence of a C IV system at the same redshift and with a similar velocity

[1] https://elt.eso.org

Table 1. The high-resolution UVES/HIRES sample. The different columns report: the name of the object, the emission redshift, the minimum and maximum redshift considered for the Si IV absorption lines to be part of the sample, the SNR per resolution element computed at $\lambda_{rest} \sim 1380$ Å, and the reference paper.

Object	z_{em}	z_{min}	z_{max}	SNR	Ref.
HE 1341−1020	2.142	1.749	2.090	200	1
QSO B0122−379	2.200	1.801	2.147	114	1
PKS 1448−232	2.224	1.821	2.171	113	1
PKS 0237−230	2.233	1.829	2.179	283	1
HE 0001−2340	2.267	1.859	2.213	190	1
QSO B1626+6426	2.320	1.905	2.265	128	5
HE 1122−1648	2.400	1.975	2.344	314	1
QSO B0109−3518	2.406	1.980	2.349	119	1
HE 2217−2818	2.414	1.988	2.357	246	1
QSO B0329−385	2.437	2.008	2.380	75	1
HE 1158−1843	2.448	2.017	2.391	97	1
HE 1347−2457	2.599	2.149	2.539	313	1
QSO B1442+2931	2.660	2.203	2.599	107	5
QSO B0453−423	2.669	2.211	2.608	194	1
PKS 0329−255	2.696	2.234	2.635	97	1
QSO J0103+1316	2.721	2.256	2.659	218	4
HE 0151−4326	2.763	2.293	2.701	182	1
QSO B0002−422	2.769	2.298	2.707	211	1
HE 2347−4342	2.880	2.395	2.816	164	1
QSO B1107+4847	2.970	2.474	2.904	94	5
QSO J0407−4410	3.021	2.519	2.954	235	4
HS 1946+7658	3.058	2.551	2.991	156	1
HE 0940−1050	3.093	2.582	3.025	333	1,2
QSO B0420−388	3.126	2.610	3.057	138	1
QSO B0636+6801	3.180	2.658	3.111	107	5
QSO B1425+6039	3.180	2.658	3.111	140	5
QSO B1209+0919	3.291	2.755	3.220	30	3
PKS 2126−158	3.292	2.756	3.221	198	1
QSO B1422+2309	3.623	3.046	3.546	90	1,5
SDSS J1249−0159	3.630	3.052	3.553	85	3
QSO B0055−269	3.660	3.078	3.583	142	1
SDSS J1621−0042	3.710	3.122	3.632	159	3,4
QSO J1320−0523	3.717	3.128	3.639	154	3
PKS 1937−101	3.787	3.189	3.708	138	1,4
QSO J1646+5514	4.100	3.463	4.016	119	5
QSO B1055+4611	4.15	3.507	4.065	47	5
QSO B2237−0608	4.56	3.866	4.468	42	5

Notes. 1: D'Odorico et al. (2010); 2: D'Odorico et al. (2016); 3: Calura et al. (2012); 4: This work; 5: BS15.

profile to confirm the identification. To avoid contamination from absorption systems associated with the quasars, we considered only absorbers with a maximum redshift, z_{max}, at a separation $\Delta v = -5000$ km s^{-1} from the quasar emission redshift. On the other hand, the contamination from Ly α lines was prevented by taking a minimum redshift, z_{min}, at a separation $\Delta v = +1000$ km s^{-1} from the Ly α emission of the quasar. The considered redshift intervals are reported in Tables 1, 2, and 3.

All the detected Si IV absorption lines were fitted with Voigt profiles mainly with the FITLYMAN context of the ESO MIDAS package (Fontana & Ballester 1995). Exceptions are discussed in the sections dedicated to the sample description.

The number of spectra per redshift bin of $\Delta z = 0.2$ for the three samples, is shown in Fig. 1.

2.1 The high-resolution UVES/HIRES sample

This sample collects the high-resolution ($R \simeq 50\,000$, $\Delta v \simeq 6.0$ km s^{-1}) spectra obtained with the UV and Visual Echelle Spectrograph (UVES) at the ESO Very Large Telescope (VLT) and with HIRES at Keck, analysed in D'Odorico et al. (2010) and Calura et al. (2012). For the quasar HE 0940−1050, we used the higher SNR spectrum presented in D'Odorico et al. (2016). Details of the data reduction and analysis are reported in D'Odorico et al. (2010).

Also, we used updated spectra (including new observations) of SDSS J1621−0042 and PKS 1937−101 and added the new spectra of QSO J0407−4410 and QSO J0103+1316. The four new spectra were reduced by E. Pomante in the context of his PhD thesis work,[2] with a custom made pipeline able to ingest both UVES and HIRES raw frames and treat them in the same way. This generalized pipeline is an extension of the IDL code developed by S. Burles and J. X. Prochaska for the reduction of MIKE and HIRES data (Bernstein, Burles & Prochaska 2015), with a modified approach to wavelength calibration, flat-fielding, and object extraction.

In order to increase the statistical significance of our sample and the coverage toward higher redshifts, we have considered also the sample of nine objects analysed in BS15, which have a similar resolution element of $\Delta v \simeq 6.6$ km s^{-1}. For the quasar spectrum of B1422+231, which is in common between our sample and BS15, we considered our list of lines, which is consistent with the BS15 one.

Note that the majority of the quasars in this sample belongs to the UVES Large Programme by Bergeron et al. (2004) which required Ly α forests free from Damped Lyman α systems (DLAs). We have thus verified the presence of DLAs in the additional quasars and excised from the final sample the redshift ranges of the corresponding Si IV lines. In particular, there is a DLA per line of sight in the BS15 spectra of QSO B1425+6039, QSO B1055+4611, and QSO B2237−0607.

The final high-resolution sample is then formed by 37 objects and covers the Si IV redshift range $1.75 \lesssim z \lesssim 4.47$, with a total scanned absorption path of $\Delta X \simeq 54$. In Table 1, we report for each object of the sample the redshift range available for Si IV detection and the SNR per resolution element of 6.6 km s^{-1} at $\lambda_{rest} \sim 1380$ Å, to be compliant with the SNR reported by BS15. The average SNR ∼156 corresponds to a 3σ detection threshold for the Si IV λ1393 Å line of $\log N(\mathrm{Si\,IV})_{thr} \simeq 11.09$ assuming a conservative $b = 10$ km s^{-1} Doppler parameter. The spectrum with the lowest SNR has $\log N(\mathrm{Si\,IV})_{thr} \simeq 11.95$.

BS15 fit absorption lines with the Voigt profile fitting code VPFIT (Carswell et al. 2014). As already shown in previous works (e.g. D'Odorico et al. 2016) there are no significant differences between the results of FITLYMAN and VPFIT. Possible differences due to, for example, an excess of low-column density components by VPFIT, are further mitigated by the fact that, as we already did in D'Odorico et al. (2010, 2013), in order to compare these high-resolution spectra with those from XSHOOTER, Si IV lines with velocity separation smaller than 50 km s^{-1} have been merged. The merging process has been carried out in the following way: For each list of Si IV components corresponding to a single quasar, the velocity separations among all the lines have been computed and sorted in ascending order. If the smallest separation is less than $dv_{min} = 50$ km s^{-1}, the two corresponding absorption lines are merged into a new line with column density equal to the sum of the column densities, and redshift equal to the average of the redshifts, weighted by the column density of the components. The velocity separations are then computed again and the procedure is iterated until the smallest separation becomes larger than dv_{min}. For consistency, the same merging process was applied to the XQ-100 sample and to the $z \sim 6$ XSHOOTER sample described in Sections 2.2 and 2.3, respectively.

[2] http://hdl.handle.net/11368/2908079

Table 2. The XQ-100 quasar sample. The columns are the same as in Table 1 with the exception of the reference column, since all the spectra were presented in López et al. (2016) and the column R_{new} which reports the adopted resolving power if different from the nominal one.

Object	z_{em}	z_{min}	z_{max}	R_{new}	Object	z_{em}	z_{min}	z_{max}	R_{new}
J1332+0052	3.5082	2.9453	3.4336	–	J0211+1107	3.9734	3.3524	3.8911	10 700
J1018+0548	3.5154	2.9516	3.4407	10 400	J0214−0518	3.9770	3.3556	3.8947	9400
J1201+1206	3.5218	2.9572	3.4470	13 400	J1032+0927	3.9854	3.3629	3.9029	10 300
J1024+1819	3.5243	2.9594	3.4495	9800	J1542+0955	3.9863	3.3637	3.9038	10 400
J1442+0920	3.5319	2.9660	3.4569	9900	J2215−1611	3.9946	3.3710	3.9120	15 000
J0100−2708	3.5459	2.9783	3.4707	9900	J0255+0048	4.0033	3.3786	3.9205	10 400
J1517+0511	3.5549	2.9862	3.4796	–	J0835+0650	4.0069	3.3817	3.9241	11 600
J1445+0958	3.5623	2.9926	3.4868	10 300	J0311−1722	4.0338	3.4053	3.9505	9700
J1202−0054	3.5924	3.0190	3.5164	–	J1323+1405	4.0537	3.4227	3.9701	10 100
J1416+1811	3.5928	3.0193	3.5168	–	J0244−0134	4.0546	3.4235	3.9710	12 000
J1524+2123	3.6002	3.0258	3.5241	–	J0415−4357	4.0732	3.4397	3.9893	9900
J1103+1004	3.6070	3.0318	3.5308	–	J0048−2442	4.0827	3.4481	3.9986	11 400
J1117+1311	3.6218	3.0447	3.5453	–	J0959+1312	4.0916	3.4558	4.0074	–
J1037+2135	3.6260	3.0484	3.5495	–	J0121+0347	4.1252	3.4852	4.0404	–
J1249−0159[a]	3.6289	3.0509	3.5523	–	J0003−2603	4.1254	3.4854	4.0406	–
J1042+1957	3.6302	3.0521	3.5536	–	J1037+0704	4.1271	3.4869	4.0423	–
J1126−0126	3.6346	3.0559	3.5579	–	J1057+1910	4.1284	3.4881	4.0436	11 800
J0056−2808	3.6347	3.0560	3.5580	–	J0747+2739	4.1334	3.4924	4.0485	–
J1020+0922	3.6401	3.0607	3.5633	9900	J1110+0244	4.1456	3.5031	4.0605	9700
J0920+0725	3.6465	3.0663	3.5696	10 100	J0132+1341	4.1523	3.5090	4.0671	9700
J1304+0239	3.6481	3.0677	3.5712	–	J2251−1227	4.1575	3.5135	4.0722	15 000
J0818+0958	3.6564	3.0750	3.5794	11 400	J0529−3552	4.1717	3.5259	4.0862	10 700
J0057−2643[a]	3.6608	3.0788	3.5837	9700	J0030−5129	4.1729	3.5270	4.0873	–
J0755+1345	3.6629	3.0807	3.5858	–	J0133+0400	4.1849	3.5375	4.0991	12 000
J1053+0103	3.6634	3.0811	3.5863	–	J0153−0011	4.1948	3.5462	4.1089	–
J1108+1209	3.6789	3.0947	3.6015	9500	J2349−3712	4.2192	3.5675	4.1329	9700
J1421−0643	3.6885	3.1031	3.6109	–	J0403−1703	4.2267	3.5741	4.1402	12 900
J1503+0419	3.6919	3.1061	3.6143	–	J0839+0318	4.2298	3.5768	4.1433	9500
J0937+0828	3.7035	3.1162	3.6257	10 200	J0247−0556	4.2335	3.5800	4.1469	–
J1352+1303	3.7065	3.1188	3.6286	–	J0117+1552	4.2428	3.5882	4.1561	–
J1621−0042[a]	3.7112	3.1229	3.6333	–	J2344+0342	4.2484	3.5931	4.1616	10 500
J0833+0959	3.7162	3.1273	3.6382	9300	J1034+1102	4.2691	3.6112	4.1819	9100
J1320−0523[a]	3.7172	3.1282	3.6392	9100	J0034+1639	4.2924	3.6316	4.2049	–
J1248+1304	3.7210	3.1315	3.6429	–	J0234−1806	4.3046	3.6423	4.2169	–
J1552+1005	3.7216	3.1320	3.6435	10 400	J0113−2803	4.3145	3.6509	4.2266	11 500
J1312+0841	3.7311	3.1404	3.6528	10 400	J0426−2202	4.3289	3.6635	4.2408	–
J0935+0022	3.7473	3.1545	3.6688	–	J1058+1245	4.3413	3.6744	4.2529	–
J1658−0739	3.7496	3.1565	3.6710	–	J1633+1411	4.3650	3.6951	4.2763	10 400
J1126−0124	3.7650	3.1700	3.6862	–	J0525−3343	4.3851	3.7127	4.2960	12 800
J1336+0243	3.8009	3.2014	3.7215	11 400	J1401+0244	4.4078	3.7326	4.3183	12 200
J1013+0650	3.8086	3.2082	3.7291	14 400	J0529−3526	4.4183	3.7418	4.3287	9500
J1135+0842	3.8342	3.2306	3.7542	–	J0955−0130	4.4185	3.7419	4.3289	10 150
J0124+0044	3.8368	3.2329	3.7568	–	J0248+1802	4.4390	3.7599	4.3490	12 000
J1331+1015	3.8522	3.2463	3.7719	11 400	J0006−6208	4.4400	3.7607	4.3500	–
J0042−1020	3.8629	3.2557	3.7825	11 600	J0714−6455	4.4645	3.7822	4.3741	15 000
J1111−0804	3.9225	3.3079	3.8411	13 400	J2216−6714	4.4793	3.7951	4.3887	9700
J0800+1920	3.9481	3.3303	3.8663	–	J1723+2243	4.5310	3.8404	4.4395	–
J1330−2522	3.9485	3.3306	3.8666	11 300	J1036−0343	4.5311	3.8405	4.4396	10 300
J0137−4224	3.9709	3.3502	3.8887	–	J2239−0552	4.5566	3.8628	4.4647	–
J1054+0215	3.9709	3.3502	3.8887	11 300	J0307−4945	4.78	4.0583	4.6844	10 300

2.2 The XQ-100 sample

XQ-100 is a collection of 100 XSHOOTER spectra of quasars with $z_{em} \simeq 3.5$–4.5 observed in the context of the ESO Large Programme 'Quasars and their absorption lines: a legacy survey of the high-redshift Universe with VLT/X-shooter' (P.I. S. López). The list of objects is reported in Table 2. The sample spans the Si IV redshift interval $2.94 \leq z \leq 4.70$.

Spectra were obtained with a binning × 2 along the dispersion direction and a slit of 0.9 arcsec in the visible arm (VIS, where all the Si IV lines fall) corresponding to a nominal resolving power of $R \sim 8900$. Data reduction was carried out with a custom pipeline, while the manually placed continuum was determined by selecting points along the quasar continuum free of absorption (by eye) as knots for a cubic spline. A total of 90 per cent of the spectra has SNR ≥20 per pixel of 11 km s^{-1} at 1700 Å rest frame. All the details can be found in López et al. (2016).

Our Si IV line sample was built based on Perrotta et al. (2016) and Berg et al. (2021). We revised those detections and fitted them with Voigt profiles, using the FITLYMAN context of the ESO MIDAS package (Fontana & Ballester 1995). During the line-fitting process,

Table 3. The XSHOOTER $z \sim 6$ sample. The columns are the same as in Table 1.

Object	z_{em}	z_{min}	z_{max}	R_{new}	Ref.
SDSS J0836+0054	5.810	4.960	5.697	13 100	1
ULAS J0148+0600	5.98	5.108	5.864	13 300	2, 3
SDSS J1306+0356	6.0337	5.155	5.917	12 000	1
SDSS J0818+1722	6.02	5.143	5.904	11 000	1
CFHQS J1509−1749	6.1225	5.233	6.005	11 800	1
ULAS J1319+0950	6.1330	5.242	6.015	13 700	1
SDSS J1030+0524	6.308	5.395	6.187	12 300	1
ATLAS J025−33	6.3379	5.422	6.216	11 200	3
VDES J0224−4711	6.526	5.586	6.401	11 200	3
PSO J036+03	6.5412	5.599	6.416	10 700	3

Notes. 1: D'Odorico et al. (2013); 2: Codoreanu et al. (2018); 3: This work.

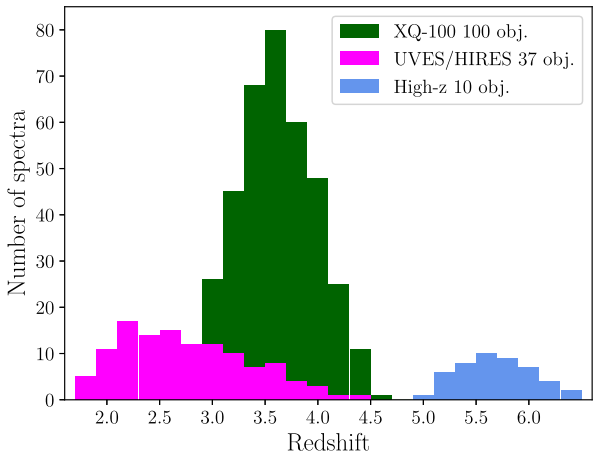

Figure 1. Number of spectra used in this work per redshift bin of $\Delta z = 0.2$.

we realized that many spectra had a resolving power significantly larger than the nominal one. As a consequence, we recomputed the value of R for each spectrum based on the average value of the seeing during the observations (reported in the ESO archive as *DIMM*) and assuming a linear relation between resolving power and slit width (equivalent in this case to the seeing average value). If $\langle DIMM \rangle < 0.9$ arcsec, the new resolving power is obtained as $R_{new} \sim (0.9/\langle DIMM \rangle) \times 8800$. The new resolving powers adopted in the fit are reported in Table 2. The resolution element varies between ∼20 and 34 km s^{-1}.

For consistency with the high-resolution sample, we excluded from the XQ-100 Si IV collection those systems which are associated with the known DLAs studied in Berg et al. (2016). Our fiducial sample covers an absorption path of $\Delta X \simeq 221.8$ for a total of 385 detected Si IV absorption lines with $\log N(\mathrm{Si\,IV}) \geq 12.5$. In the following, this sample will be called 'XQ-100-noDLA'. We verified that the results are not significantly affected by the inclusion or exclusion of the Si IV lines associated with the DLAs.

2.3 The $z \sim 6$ XSHOOTER sample

This is a collection of 10 XSHOOTER quasar spectra of which: six were already analysed in D'Odorico et al. (2013). ULAS J0148+0600 was analysed in Codoreanu et al. (2018) but we re-analysed the XSHOOTER spectrum in the ESO archive, and the last three spectra are published in this paper for the first time. The sample is reported in Table 3 and the log of observation for the new objects is in Table 4. In this sample, the Si IV is observable in the redshift range $4.96 \leq z \leq 6.40$. As for the XQ-100 sample, we have revised the resolution of the spectra based on the atmospheric conditions in which they were observed. The new resolving powers are reported in Table 3.

Table 4. Log of observations for the three new quasars at $z > 6.3$ observed with XSHOOTER. Columns 2 and 4 report the cumulative exposure time per target, per run. While columns 3 and 5 report the adopted slit width. They correspond to nominal resolving powers of $R \simeq 8900$ for 0.9 arcsec in the VIS, and $R \simeq 5600$ (8100) for 0.9 arcsec (0.6 arcsec) in the Near Infra-Red (NIR) arm.

Programme	Exp. T_{VIS} (s)	slit$_{VIS}$ (arcsec)	Exp. T_{NIR} (s)	slit$_{NIR}$ (arcsec)
ATLAS J025.6821−33.4627				
P096.A−0418[a]	5580	0.9	5760	0.9JH
P0102.A−0154[b]	14160	0.9	14400	0.6
VDES J0224−4711				
P0100.A−0625[b]	4640	0.9	4800	0.9
P0102.A−0154[b]	4720	0.9	4800	0.6
P1103.A−0817[b]	24000	0.9	24000	0.6
PSO J036.5078+03.0498				
P0100.A−0625[b]	4640	0.9	4800	0.9
P0102.A−0154[b]	18880	0.9	19200	0.6

Notes. [a] P.I. T. Shanks. [b] P.I. V. D'Odorico.

The three new quasars were reduced with the custom pipeline used for the XQ-100 spectra and analysed with the python-based software ASTROCOOK[3] (Cupani et al. 2020). We carried out line detection, continuum determination, and then line identification and Voigt profile fitting in the context of ASTROCOOK. For consistency, we used ASTROCOOK also to repeat the fit of the absorption lines in the other quasars of the sample. The line parameters obtained with ASTROCOOK are consistent within the measurement errors with those reported in D'Odorico et al. (2013) that were obtained within the FITLYMAN context of the ESO MIDAS package (Fontana & Ballester 1995). The 10 spectra allow to probe Si IV absorption lines with $\log N(\mathrm{Si\,IV}) \geq 12.5$ along an absorption path $\Delta X \simeq 32.7$, in which a total of 22 lines have been detected.

In the following, we give a brief description of the new quasars and of the detected Si IV absorption systems, whose parameters are given in Table 5. The complete analysis of the absorption systems in the new spectra will be described in a forthcoming paper (Davies et al. in preparation).

ATLAS J025.6821−33.4627 (J0142−3327)

This object was discovered in the context of the VLT Survey Telescope (VST) ATLAS survey (Carnall et al. 2015). It has a redshift $z_{em} = 6.3379$ measured from the [C II] emission line (Decarli et al. 2018). It was observed with XSHOOTER at the VLT in 2015 October/November and in 2018 November. We detect in the spectrum several C IV absorption systems of which two, at $z = 5.64573$ and $z = 5.76781$, have also an associated Si IV absorption.

VDES J0224−4711

This quasar, at $z = 6.526$, was discovered recently (Reed et al. 2017) and is the second most luminous quasar known at $z \geq 6.5$. It was observed with XSHOOTER at the VLT in 2017 November, 2018 January, and 2019 January/December. Several C IV systems have been detected in this spectrum with that at $z = 6.030\,82$ showing an associated Si IV absorption. We detect also a possible Si IV absorption

[3] http://github.com/DAS-OATs/astrocook

Table 5. Results of the Si IV lines identification and fitting for the XSHOOTER spectra of J0148 and the three new quasars at $z > 6.3$.

z_{abs}	b (km s^{-1})	log N(Si IV)
	ULAS J0148+0600	
5.12517 ± 0.00002	27. ± 2	12.77 ± 0.02
5.48778 ± 0.00003	24. ± 2	12.77 ± 0.03
	ATLAS J025.6821−33.4627	
5.64574 ± 0.00004[a]	5.0	12.23 ± 0.10
5.76786 ± 0.00004	12 ± 4	12.72 ± 0.04
	VDES J0224−4711	
5.55276 ± 0.00004[a]	26 ± 3	12.72 ± 0.03
6.03082 ± 0.00006	18 ± 5	12.95 ± 0.08
	PSO J036.5078+03.0498	
5.89873 ± 0.00006	6.0	12.67 ± 0.09
5.90223 ± 0.00001	33 ± 8	12.86 ± 0.09

Notes. [a] This line has not been considered in the analysis because its column density or redshift fall outside the considered ranges.

at $z = 5.552\,76$, the corresponding C IV transitions are not detected because they would fall in a very noisy region of the spectrum.

PSO J036.5078+03.0498 (J0226+0302)

Venemans et al. (2015) discovered this very bright quasar based on the imaging obtained by the Pan-STARRS1 Survey. The systemic redshift, $z = 6.5412$, was determined from the [C II] emission line (Decarli et al. 2018). Observations with XSHOOTER at the VLT were carried out in 2017 December, 2018 January/November, and 2019 January. In this spectrum, two systems have both C IV and Si IV lines at $z = 5.898\,69$ and $z = 5.902\,399$.

2.4 Comparison between XSHOOTER and UVES spectra

In general, Si IV absorptions are relatively weak, so even if the resolution of XSHOOTER does not allow resolving most of the metal lines, our measured column densities should not be significantly affected by unresolved saturation. To prove this statement, we have considered the Si IV absorption lines identified and fitted in the four quasars that are in common between the high-resolution sample and the XQ-100 sample: J1249−0159, Q0055−269 (or J0057−2643), J1621−0042, and J1320−0523. In order to compare the measured column densities, due to the different resolutions of the two samples, we have computed the total column density of each absorption 'system' obtained after the merging process described in Section 2.1. Results are reported in Fig. 2. All systems with column density log N(Si IV) $\gtrsim$ 12.5 have UVES and XSHOOTER measurements which are consistent within observational errors. As we will see in the following sections, our analysis will be based only on systems with log N(Si IV) $\geq$ 12.5 for which we are substantially complete given the minimum SNR of the analysed spectra; as a consequence we will assume that XSHOOTER column densities are reliable even though lines are probably not resolved in XSHOOTER spectra.

3 STATISTICS OF THE SI IV ABSORPTION LINES

3.1 Column density distribution function

The CDDF, $f(N)$, is defined as the number of lines per unit column density and per unit redshift absorption path, dX (Tytler 1987). The redshift absorption path is used to remove the redshift dependence in the sample and put everything on a comoving coordinate scale. In

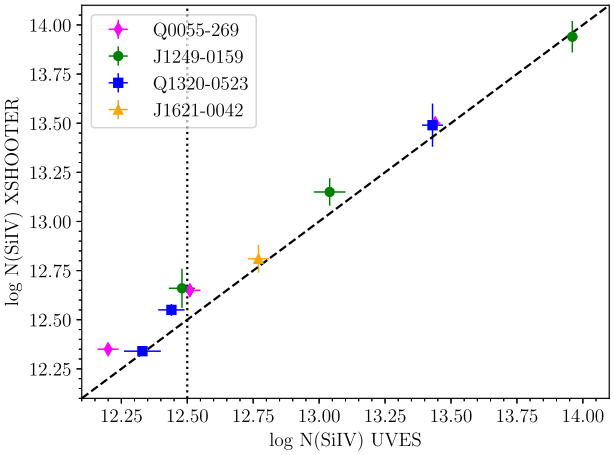

Figure 2. Comparison between the column densities obtained for the Si IV systems in the four quasars which are in common between the UVES/HIRES sample and the XQ-100 one. The vertical dotted line marks the minimum Si IV column density we adopt for our computations and the dashed line indicates the 1:1 relation.

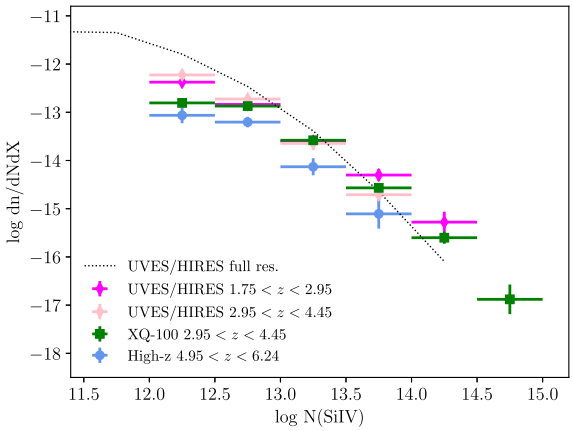

Figure 3. CDDF for the Si IV absorptions in the UVES/HIRES (pink and magenta diamonds), XQ-100 (green squares), and $z \sim 6$ XSHOOTER (blue circles) samples. The dotted line indicates the CDDF of the original UVES/HIRES sample (before merging the lines closer than 50 km s^{-1}).

the assumed cosmology it is defined as

$$dX \equiv (1+z)^2[\Omega_m(1+z)^3 + \Omega_\Lambda]^{-1/2}dz. \quad (1)$$

With the adopted definition, $f(N)$ does not evolve at any redshifts for a population whose physical size and comoving space density are constant.

The CDDF is a fundamental statistical property of absorption lines, similar for many aspects to the luminosity function for stars and galaxies.

The results of the computation of the CDDF for our three samples are shown in Fig. 3. In the figure, the CDDF of the original UVES/HIRES sample (before merging the lines closer than 50 km s^{-1}) is shown as a dotted line. The 'full resolution' sample shows an increasing CDDF, suggesting a good completeness down to the log N(Si IV) = [11.5–12.0] column density bin, and then it flattens out. These values are in agreement with the column density thresholds derived from the SNR of the spectra in Section 2.1.

We observe that the number density of lines for the two UVES/HIRES redshift bins and for XQ-100-noDLA are consistent in the column density range $12.5 \leq \log N(\mathrm{Si\,IV}) \leq 14.5$; at $\log N(\mathrm{Si\,IV}) \leq 12.5$ the different behaviour is driven by the fact that the XQ-100-noDLA sample is not complete (e.g. Ellison et al. 2000); at $\log N(\mathrm{Si\,IV}) \geq 14.5$ only the XQ-100-noDLA sample shows detected lines, attesting that these high-column density lines are rare and a large number of lines of sight are needed to detect a significant number of them.

Comparing the CDDF at $z < 4.8$ with that at $z \geq 4.8$ computed with the $z \sim 6$ XSHOOTER sample, we remark that at high z the CDDF is systematically lower than at lower z by ∼0.3–0.5 dex for all the column density bins between 12.0 and 14.0. The very low value at $12.0 \leq \log N(\mathrm{Si\,IV}) \leq 12.5$ can still be explained with the incompleteness of the sample, while the lack of lines at $\log N(\mathrm{Si\,IV}) \geq 14.5$ is consistent with the rarity of these lines and the low number of the inspected lines of sight.

In more detail, from the XQ-100-noDLA CDDF, a number density of 0.05 ± 0.01 (0.009 ± 0.006, based on two lines) in the column density bin [14.0,14.5] ([14.5,15.0]) can be derived. Based on the surveyed absorption paths, these number densities imply a number of absorption lines consistent with zero in the column density bin [14.5,15.0] for both the $z \sim 6$ XSHOOTER sample ($n = 0.3 \pm 0.2$) and the two inspected redshift bins of the UVES/HIRES sample ($n = 0.3 \pm 0.2$ and 0.2 ± 0.1). In the lower column density bin [14.0,14.5], the number of expected lines is consistent with ∼0–2 and only in the case of the UVES/HIRES lower redshift bin, $z = [1.75, 2.95]$, we actually detect one Si IV absorption line.

3.2 Number density

We have also computed the number density of Si IV absorption lines with column densities $\log N(\mathrm{Si\,IV}) \geq 12.5$ for which all samples have a high completeness rate. For all samples we have considered the Si IV systems defined as described in Section 2.1.

The number density has been computed as the number of lines (N_{lin}) in the considered redshift bin divided by the redshift absorption path (ΔX) obtained integrating equation (1) in the redshift intervals contributed by each line of sight to the specific redshift bin. The results are shown in Fig. 4 and in Table 6. The high-resolution UVES-HIRES sample shows in the redshift range $1.75 \leq z \leq 4.45$ a behaviour which is consistent with a flat evolution with a possible hint of slightly decreasing number density toward lower redshifts. The XQ-100 sample which is characterized by the largest number of lines of sight and, accordingly, of absorption lines, is in agreement with the previous sample within observational errors. The lower value in the $z = [2.95, 3.47]$ redshift bin could be marginally affected by the fact that it covers the first order of the XSHOOTER VIS spectrum, which in general has a slightly lower SNR with respect to the rest of the investigated spectrum.

Considering now the $z \sim 6$ sample, the measured number density values in the two analysed redshift bins are consistent between themselves within measured errors. On the other hand, $\mathrm{d}n/\mathrm{d}X$ at $z = [4.95, 5.65]$ is a factor of ∼2 lower than the XQ-100 $\mathrm{d}n/\mathrm{d}X$ value at $z = [3.90, 4.70]$ significant at 4.5σ, confirming that $\mathrm{d}n/\mathrm{d}X$ evolved dramatically at $z > 4$.

4 THE REDSHIFT EVOLUTION OF THE SI IV MASS DENSITY

Finally, the CDDF can be integrated in order to obtain the cosmological mass density of Si IV in QSO absorption systems as a fraction of the critical density today, or the contribution of Si IV to the closure density:

$$\Omega_{\mathrm{SiIV}} = \frac{H_0\, m_{\mathrm{SiIV}}}{c\, \rho_{\mathrm{crit}}} \int N f(N) \mathrm{d}N, \tag{2}$$

where $H_0 = 100\, h\, \mathrm{km\,s^{-1}Mpc^{-1}}$ is the Hubble constant, m_{SiIV} is the mass of a Si IV ion, c is the speed of light, $\rho_{\mathrm{crit}} = 1.88 \times 10^{-29}\, h^2\, \mathrm{g\,cm^{-3}}$, and $f(N)$ is the CDDF. The above integral can be approximated by the sum

$$\Omega_{\mathrm{SiIV}} = \frac{H_0\, m_{\mathrm{SiIV}}}{c\, \rho_{\mathrm{crit}}} \frac{\sum_i N_i(\mathrm{SiIV})}{\Delta X} \tag{3}$$

with an associated fractional variance

$$\left(\frac{\delta\Omega_{\mathrm{SiIV}}}{\Omega_{\mathrm{SiIV}}}\right)^2 = \frac{\sum_i [N_i(\mathrm{SiIV})]^2}{\left[\sum_i N_i(\mathrm{SiIV})\right]^2} \tag{4}$$

as proposed by Storrie-Lombardi, McMahon & Irwin (1996). Note that the errors determined with this formula could be underestimated, in particular in the case of small line samples. In D'Odorico et al. (2010), we found that errors on Ω_{CIV} computed with a bootstrap technique were, at maximum, a factor of ∼1.5 larger than those estimated with equation (4). For a fair comparison with previous

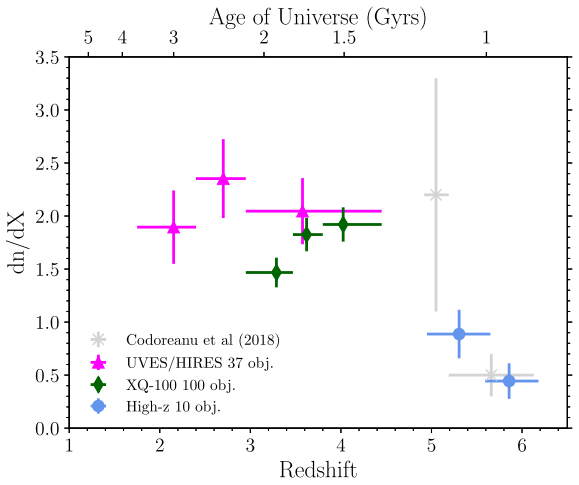

Figure 4. Number density for the Si IV absorptions detected in our three samples. Lines have been selected to have column densities $\log N(\mathrm{Si\,IV}) \geq 12.5$ and redshifts in the range $1.75 \leq z \leq 6.24$. The light grey crosses are the results from Codoreanu et al. (2018).

Table 6. Si IV number density and cosmic mass density results considering $\log N(\mathrm{Si\,IV}) \geq 12.5$.

z range	ΔX	N_{lin}	$\mathrm{d}n/\mathrm{d}X$	$\Omega(\mathrm{Si\,IV})$ ($\times 10^{-8}$)
		UVES/HIRES		
1.75–2.40	15.83	30	1.9 ± 0.3	1.9 ± 0.6
2.40–2.95	17.00	40	2.3 ± 0.4	2.3 ± 0.6
2.95–4.40	21.02	43	2.0 ± 0.3	1.1 ± 0.2
		XQ-100 noDLA		
2.95–3.47	74.96	110	1.5 ± 0.1	1.2 ± 0.2
3.47–3.80	73.42	134	1.8 ± 0.2	1.9 ± 0.5
3.80–4.45	73.43	141	1.9 ± 0.2	1.2 ± 0.2
		XSHOOTER $z \sim 6$		
4.95–5.65	16.91	15	0.9 ± 0.2	0.4 ± 0.1
5.65–6.24	15.77	7	0.4 ± 0.2	0.18 ± 0.08

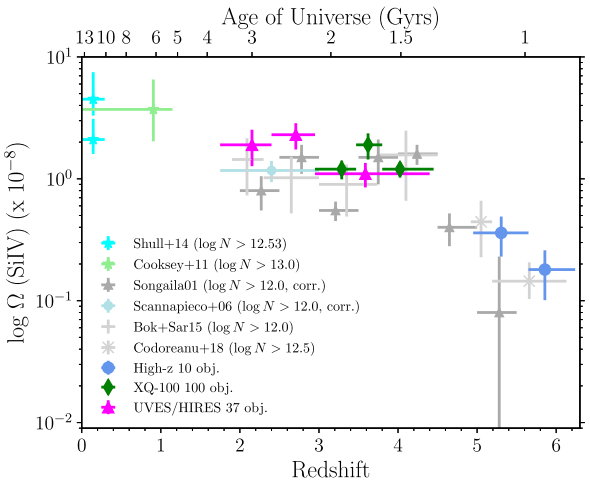

Figure 5. Cosmic mass density for the Si IV absorptions detected in our three samples. Lines have been selected to have column densities $\log N(\mathrm{Si\,IV}) \geq 12.5$ and redshifts in the range $1.75 \leq z \leq 6.24$. Also shown are results by Shull et al. (2014) and Cooksey et al. (2011) for $z \leq 1$ and, for $z \geq 1.8$, the results by Songaila (2001), Scannapieco et al. (2006), BS15, and Codoreanu et al. (2018). See the main text for further details.

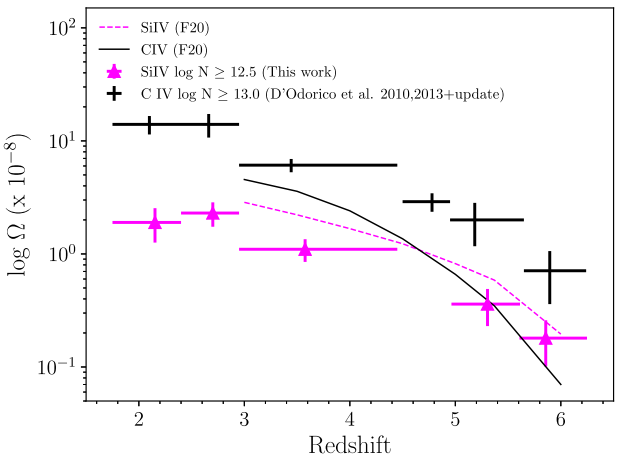

Figure 6. Comparison of the cosmic mass density parameters, Ω, for Si IV and C IV (D'Odorico et al. 2010, 2013, this work) among themselves and with the predictions of the simulations by F20.

results, however, we report in Table 6 the errors computed with equation (4).

It is interesting to point out the complementarity of the information conveyed by the number density, dn/dX, which is heavily weighted toward abundant low-column density systems, and by the cosmological mass density, Ω_{SiIV}, whose value depends mainly on the rare high-column density absorption lines.

As already observed for the CDDF and the number density of lines, Fig. 5 shows that the mass density parameter of Si IV increases by a factor ∼4–6 moving from the redshift bin $z = [4.95, 5.65]$ to $z = [3.90, 4.70]$. In the redshift interval $2.94 \leq z \leq 4.70$ the evolution of Ω_{SiIV} is consistent with a flat behaviour, with a possible further increase toward $z \sim 1$ and the local Universe.

The low-z measurements were carried out by: Cooksey et al. (2011) using *HST*/STIS, *HST*/GHRS, and FUSE data with Si IV lines in the redshift range $z \sim 0.0$–1.15 and $\log N(\mathrm{Si\,IV}) \geq 13$, and by Shull et al. (2014) using *HST*/COS spectra for Si IV lines in the redshift range $z \sim 0.0$–0.29 with $\log N(\mathrm{Si\,IV}) \geq 12.53$. The reported values correspond to two Si IV samples obtained with *HST*/STIS ($\Omega_{\mathrm{SiIV}} = 4.5^{+3.0}_{-1.2} \times 10^{-8}$) and with *HST*/COS ($\Omega_{\mathrm{SiIV}} = 2.1^{+1.0}_{-0.5} \times 10^{-8}$).

5 OUR RESULTS INTO CONTEXT

5.1 Comparison with previous Si IV results

The statistical quantity which is more safely comparable between different samples of absorption lines is the cosmic mass density, since it depends less on the resolution and the adopted fitting technique.

In Fig. 5, we report our measurements and previous determinations of Ω_{SiIV} at lower and comparable redshifts. Our results are in good agreement with the Songaila (2001) data, corrected for the different cosmology (see also Songaila 2005, based on the pixel optical depth technique).

Scannapieco et al. (2006) analysed a sample of 19 UVES spectra which are included in our high-resolution sample and give in their paper a value of $\Omega_{\mathrm{SiIV}} = (0.6 \pm 0.12) \times 10^{-8}$ at $\langle z \rangle = 2.4$, which is alarmingly lower than our result. A careful revision of their paper revealed a mistake in the computation of the normalization factor of Ω_{SiIV} whose correction determines the new value $1.17 \pm 0.23 \times 10^{-8}$, consistent with our points.

The cosmic mass density for Si IV computed by BS15 is based on a sample of nine high-resolution *Keck*/HIRES quasar spectra. We have included the quasars lines of sight of BS15 in our sample, with the aim of extending the high-redshift coverage. This is reflected in Fig. 5 by the optimal consistency between our points and those of BS15.

Codoreanu et al. (2018) computed the statistical properties of Si IV absorption lines approaching $z \sim 6$. They considered a sample of four quasars all observed with XSHOOTER: ULAS J0148+0600, SDSS J1306+0356, ULAS J1319+0950 which are also part of our sample, and SDSS J0927+2001 ($z_{\mathrm{em}} = 5.79$). They found seven Si IV systems with column density $\log N(\mathrm{Si\,IV}) \geq 12.5$ in the redshift range $4.92 \leq z \leq 6.13$, of which five have $z \geq 5.19$. As we can see from Figs 4 and 5 our results are consistent with their findings within the observational errors.

5.2 Comparison with C IV and O I statistics

The statistical properties of C IV lines were the first to be studied thanks to the large available samples. In D'Odorico et al. (2013), we investigated the evolution with redshift of the C IV CDDF and cosmic mass density parameter up to $z \sim 6$. Both quantities increase significantly between $z \sim 6$ and 5 and then stay approximately constant in the range $2.0 \lesssim z \lesssim 5.0$. More recent studies (Codoreanu et al. 2018; Meyer et al. 2019) confirm these results.

The cosmic mass densities of Si IV absorbers with $\log N \geq 12.5$ estimated in this work and of C IV systems with $\log N(\mathrm{C\,IV}) \geq 13.0$ are compared in Fig. 6. The choice of the C IV column density threshold depends on the Si IV column density threshold and on the observation that, in particular at $z \gtrsim 5$, the average ratio of Si IV/C IV column densities in log is ∼−0.5 (D'Odorico et al. 2013). Ω_{CIV} has been computed in the same redshift bins adopted for Ω_{SiIV} and it is based on the UVES/HIRES sample from D'Odorico et al. (2010) and on the $z \sim 6$ XSHOOTER sample from D'Odorico et al. (2013). The $z \sim 6$ XSHOOTER sample has been updated with the addition of the C IV lines of ULAS J0148+0600 (Codoreanu et al. 2018) and of

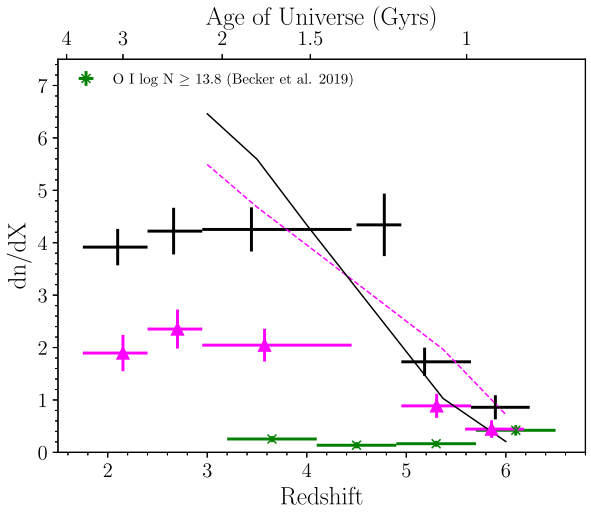

Figure 7. Number densities, dn/dX, of O I (green crosses, Becker et al. 2019), Si IV, and C IV (D'Odorico et al. 2010, 2013, this work) as a function of redshift, compared with the predictions for Si IV and C IV by F20. Symbols and lines are the same of Fig. 6.

those of the three new quasars analysed in this work.[4] The values of the computed number density and cosmic mass density for C IV are reported in Table 7. The two cosmic mass densities evolve with redshift in a very similar way, with an approximately constant ratio in the whole redshift range.

In Fig. 7, we compare dn/dX for Si IV absorbers with $\log N \geq 12.5$, estimated in this work, with the number densities of O I systems with $\log N(\mathrm{O\,I}) \geq 13.8$ (Becker et al. 2019) and C IV absorbers with $\log N(\mathrm{C\,IV}) \geq 13.0$. Si IV traces the C IV behaviour quite closely at all redshifts, with on average a factor ∼2 less lines in each redshift bin. The increase of dn/dX with decreasing redshift for C IV is generally ascribed to the combination of the increase of the ionization status and the increase of the average metallicity of the gas, as we approach the peak of star formation (e.g. Finlator et al. 2015; Maiolino & Mannucci 2019). On the other hand, O I shows a decrease at $z < 5.7$, then a constant behaviour to $z = 4$, and a possible increase for $z < 4$. The decrease of O I number density at $z < 5.7$ can only be explained by a variation in the physical properties of the gas that is transitioning from a relatively neutral state to higher ionization states (Doughty & Finlator 2019).

The fact that Si IV and O I number densities coincide in the highest redshift bin does not imply that they trace the same absorbers, this is seen when inspecting absorption systems in our sample and also in other works (e.g. Becker et al. 2019). A detailed analysis of the column density ratios of different ions in the same absorption systems will be carried out in a further work. It is interesting to see the sudden increase of the C IV number density in the redshift bin $z = [4.5, 4.95]$, which unfortunately cannot be covered by the present Si IV sample.

5.3 Comparison with simulation predictions

We now compare our results on the evolving Si IV and C IV abundances against the predictions from the four cosmological hydrodynamic simulations in the literature which computed the Si IV observables we have measured. For reference, we have summarized the simulations' relevant physical and numerical parameters in Table 8.

Large box sizes account more completely for the rare, high-column density systems that dominate Ω_{SiIV} and Ω_{CIV}, while high mass resolution accounts more completely for the weak systems that dominate dn/dX (Keating et al. 2016; F20). Note that an increase of the mass-loading factor[5] suppresses the star-formation efficiency and the CGM metallicity, decreasing the abundance of high-ionization metal absorbers (R16). On the other hand, the wind speed regulates the ability of galactic outflows to heat the CGM as well as the fraction of ejecta that travels to the virial radius. The predicted CGM metallicity is proportional to the metal yield, which is uncertain by roughly a factor of two (Wiersma et al. 2009).

O09 extract absorber catalogues using a homogeneous UVB (HM01) and a 'bubble' model in which the UVB is determined by the nearest galaxy. Comparing with their fig. 11, both models overpredict Ω_{SiIV} at $z \sim 5$ and 6 by 2–3σ. By contrast, they are in good agreement with Ω_{CIV} at the same redshifts. These results could indicate that the assumed silicon yield is too high. Alternatively, they could indicate that the overall CGM metallicity is too high owing to O09's low mass-loading factor. In this case, the agreement with Ω_{CIV} would indicate that the adopted HM01 UVB is weak at the

Table 7. C IV number density and cosmic mass density results for the high-resolution sample (D'Odorico et al. 2010) and for the XSHOOTER $z \sim 6$ sample (D'Odorico et al. 2013, this work) considering column densities $\log N(\mathrm{C\,IV}) \geq 13.0$ and adopting the same redshift bins used for Si IV with the exception of the bin $z = [4.50, 4.95]$ which is only covered for C IV absorptions.

z range	ΔX	N_{lin}	dn/dX	Ω(C IV) ($\times 10^{-8}$)
		UVES/HIRES		
1.75–2.40	32.43	127	3.9 ± 0.3	14 ± 3
2.40–2.95	21.32	90	4.2 ± 0.4	14 ± 3
2.95–4.45	23.98	102	4.2 ± 0.4	6.1 ± 0.8
		XSHOOTER $z \sim 6$		
4.50–4.95	12.21	53	4.3 ± 0.6	2.9 ± 0.5
4.95–5.65	23.73	41	1.7 ± 0.3	2.0 ± 0.8
5.65–6.24	16.28	14	0.9 ± 0.2	0.7 ± 0.3

Table 8. Our comparison simulations. The different columns report: the simulation reference (see text), the box size, the number of gas resolution elements when the simulation starts, the model for the ultraviolet ionizing background, the mass-loading factor, the wind velocity for a $M_{\mathrm{b}} = 10^9$ M$_\odot$ galaxy at $z = 5$, and the cosmological power-spectrum normalization.

Ref.	Box	N_{gas}	UVB	η_{10}	v_{wind}	σ_8
	(h^{-1} Mpc)		(km s^{-1})		(h^{-1} Mpc)	
1	16	512^3	5	3.96	82.3	0.83
2	18	512^3	6	11.3	110.9	0.816
3	100	1504^3	5	–	–	0.8288
4	15	640^3	–	6.47	104	0.8159

Notes. 1: Oppenheimer, Davé & Finlator (2009, hereafter O09); 2: G17; 3: R16; 4: Finlator et al. (2020, hereafter F20); 5: Haardt & Madau (2001, hereafter HM01); 6: Haardt & Madau (2012).

[4]The corresponding lists of C IV absorbers are reported in Table A1.

[5]The mass-loading factor, η_{10}, quantifies the ratio of the rate at which a galaxy ejects its interstellar medium to its star-formation rate.

high energies that regulate C IV, cancelling the effect of the high metallicity.

The reference simulation of R16 incorporates a lower mass resolution and a larger cosmological volume than the other three models, making it less complete for weak systems and more complete for strong ones. Its feedback model enables galactic outflows to form self-consistently, hence the mass-loading factor and wind velocities are not parametrized (Dalla Vecchia & Schaye 2012). The predicted redshift evolution of both the Si IV CDDF and $\Omega_{\rm SiIV}$ are in qualitative agreement with our observations. By contrast, both quantities are underpredicted for C IV, particularly at $z > 3.5$. Our results confirm that this C IV underprediction, previously noted by R16, does not reflect observational sample size limitations. In analogy with our conclusions from O09, we find that either the assumed carbon yield is too low (at $z > 3.5$), or the predicted overall CGM metallicity is realistic while the HM01 UVB is, as in the case of O09, too weak at high energies.

In the fiducial model of G17, the high mass-loading factor suppresses star formation and hence the CGM metallicity. On the other hand, the high wind speeds heat the CGM efficiently. We therefore expect a partial cancellation between the impacts of low metallicity and high temperature on high-ionization CGM absorbers. Codoreanu et al. (2018) find that the Si IV CDDF predicted by this model agrees with their observations in the redshift bin $z = [4.92, 6.13]$ up to column densities of $\log N(\text{Si IV}) = 13.5$, while possibly overproducing stronger systems. The higher column densities probed by our study enable us to confirm that the G17 Si IV CDDF is too flat, overpredicting observations at column densities exceeding $\log N(\text{Si IV}) \sim 14$. $\Omega_{\rm SiIV}$ is consequently overpredicted by roughly an order of magnitude when integrating over columns up to $\log N(\text{Si IV}) = 15$. The predicted redshift evolution of $\Omega_{\rm SiIV}$ may also be more gradual than observed: G17 predict that it drops by $\approx 2 \times$ from $z = 4 \rightarrow 6$ (fig. 8 of Codoreanu et al. 2018), whereas our observations indicate a factor $\sim$2.5–5 decline over the same interval. Much of this decline occurs at $z > 5$, where observations remain the most challenging.

Finally, the simulation by F20 combines a feedback model in which the adopted wind speeds and mass-loading factor are intermediate between G17 and O09 with a treatment for a self-consistent, spatially inhomogeneous UVB that yields a realistic reionization history and post-reionization UVB amplitude.

Comparisons with D'Odorico et al. (2013) showed that under the assumption of ionization-bounded escape (see e.g. Zackrisson, Inoue & Jensen 2013; F20), the predictions by F20 underproduce strong C IV absorbers while roughly reproducing strong Si IV absorbers. The improved Si IV sample presented in this work confirms the result of F20. The missing C IV and Si IV gas is found in lower ionization states. Indeed, F20 show that increasing ionization (density-bounded model) improves the agreement with the observed C IV and Si IV CDDF but worsens the agreement with the C II absorber statistics (their fig. 7).

Fig. 6 shows that, at all redshifts, the F20 simulation accounts for the overall Si IV mass density. The predicted $\Omega_{\rm SiIV}$ normalization is slightly high, but this offset falls within the range of uncertainty associated with the unknown metal yields. By contrast, the predicted $\Omega_{\rm CIV}$ evolution is steeper than observed, suggesting that the model cannot account for the observed early assembly of strong C IV systems.

Fig. 8 reveals that the predicted Si IV CDDF is somewhat too steep, overproducing faint absorbers to a degree that increases with time (also seen in Fig. 7). Further work will be required to determine what portion of this discrepancy reflects observational incompleteness, which manifests as a clear flattening in the observed Si IV CDDF for $\log N(\text{Si IV}) < 12.5$. The C IV CDDF is likewise too steep. At $z > 4$, this problem is compensated by its low normalization, leading to tolerable agreement with the observed dn/dX (see Fig. 7). At $z < 4$, the overabundance of weak C IV systems causes the model to overproduce dn/dX, in agreement with results from a complementary study that focused on the observed C IV equivalent width distribution (Hasan et al. 2020).

6 SUMMARY

In this paper, we have computed the statistical properties of a sample comprising almost 600 Si IV absorption lines with column densities $\log N(\text{Si IV}) \geq 12.5$, detected in the spectra of 147 quasars at redshifts between $2.1 \lesssim z_{\rm em} \lesssim 6.5$.

The main results of this work are the following:

(i) The CDDF of Si IV absorption lines does not show significant variations in the redshift range $1.7 \lesssim z \lesssim 4.7$, while for the highest redshift bin $4.95 \leq z \leq 6.24$ it is systematically lower at all column densities (Fig. 3). The same behaviour was observed for C IV absorption lines (e.g. D'Odorico et al. 2013).

(ii) The number density of lines per unit redshift absorption path, dn/dX, shows a small increase with redshift between $z \sim 6$ and $z \sim 5.3$ and then a jump of a factor $\sim$2.5 at $z < 4.7$. Then, the number density remains approximately constant to $z \sim 2$.

(iii) The comparison of the number densities of Si IV, C IV, and O I shows that Si IV lines with $\log N(\text{Si IV}) \geq 12.5$ and C IV lines with $\log N(\text{C IV}) \geq 13.0$ have a very similar evolution with redshift, while O I shows a mild decrease for $z < 5.7$ as reported in Becker et al. (2019).

(iv) The Si IV cosmic mass density shows a smooth increase from redshift $\sim$6 to 3.5 (of a factor $\sim$5) and then it stays constant to $z \sim 2$.

(v) The comparison of $\Omega_{\rm SiIV}$ with $\Omega_{\rm CIV}$ shows a similar evolution in redshift with an almost constant ratio.

(vi) Finally, the examination of the predictions from cosmological, hydro-dynamical simulations indicates that the observed CDDF and cosmic mass density of Si IV are well reproduced when the same quantities for C IV are underpredicted. In those cases in which feedback (or other properties) are boosted to reproduce C IV, the Si IV mass density is generally overproduced. The C IV line incidence predicted by F20 is generally consistent with observations while the Si IV line incidence is roughly consistent with observations at $z = 6$ but then grows too rapidly down to at least $z = 3$. Meanwhile, the predicted C IV CDDF of the F20 model is too steep, particularly at early times, while the Si IV CDDF has roughly the correct shape.

The results presented in this work probe new observational ground to constrain future models and advance our understanding of the distribution of metals and the enrichment mechanism of CGM and IGM.

At $z \gtrsim 5$, we are still dealing with low number statistics and the results are relatively uncertain. This problem should soon be solved by the XQR-30 survey that will provide a sample of 30 new QSO spectra in the redshift range $z_{\rm em} = 5.8$–6.6 obtained with XSHOOTER at the *VLT* in the context of an ESO Large Programme (1103.A-0817, P.I. V. D'Odorico) whose observations are almost complete.

In the longer run, when high-resolution spectrographs will be available at 30–40 m class telescopes (e.g. Marconi et al. 2021) it will be possible to carry out more detailed studies on $z \sim 6$ metal absorption lines with the resolution and column density ranges

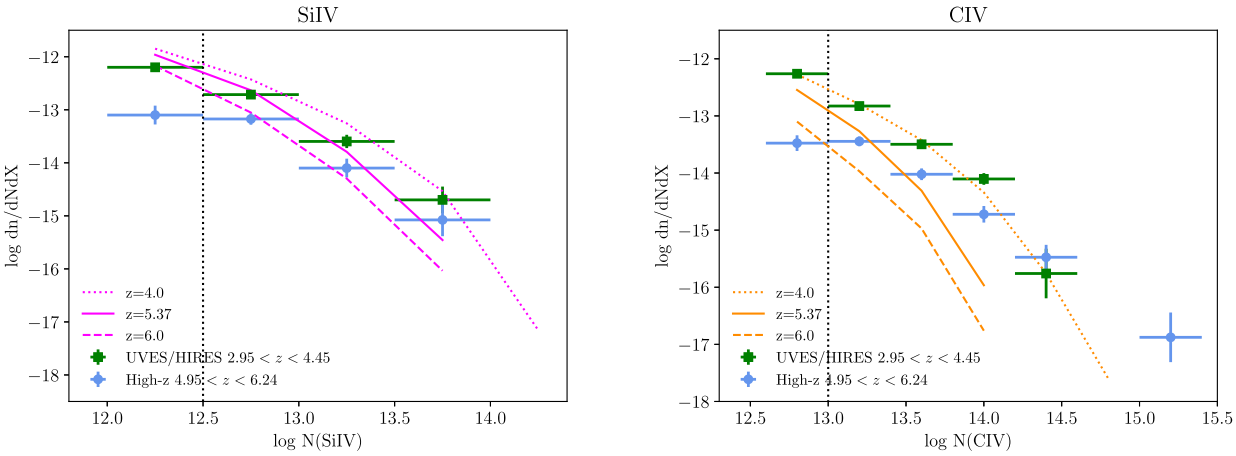

Figure 8. Predictions by F20 for the CDDF of absorbers at three different redshifts, $z = 4.0$, 5.37, and 6, compared with: (Left-hand panel) the CDDF of the Si IV absorbers in the UVES/HIRES sample (green squares) and in the high-z sample (light blue circles) and (Right-hand panel) the CDDF of the C IV absorbers in the high-resolution sample from D'Odorico et al. (2010, green squares) and in the high-z sample (D'Odorico et al. 2013, this work, light blue circles).

reachable today with 8–10 m class telescope at $z \sim 2$–4. Doughty et al. (2018) have shown that larger ranges in column densities for C IV and Si IV will allow to better distinguish between different UVB models at $z \sim 6$.

ACKNOWLEDGEMENTS

We are thankful to the anonymous referee who has provided insightful comments to the paper allowing us to improve it sensibly. This work is based in part on observations collected at the European Southern Observatory Very Large Telescope, Cerro Paranal, Chile - Programmes 65.O-0296, 166.A-0106, 069.A-0529, 079.A-0226, 084.A-0390, 084.A-0550, 085.A-0299, 086.A-0162, 087.A-0607, 268.A-5767, 189.A-0424, 096.A-0418, 0100.A-0625, 0102.A-0154, 0103.A-0817, and 1103.A-0817. Further observations were made at the W.M. Keck Observatory, which is operated as a scientific partnership between the California Institute of Technology and the University of California; it was made possible by the generous support of the W. M. Keck Foundation. The authors wish to recognize and acknowledge the very significant cultural role and reverence that the summit of Maunakea has always had within the indigenous Hawaiian community. SL acknowledges support by FONDECYT grant 1191232. KF acknowledges support from the National Science Foundation (NSF) via Award Number 2006550. The Technicolor Dawn simulations were enabled by the Extreme Science and Engineering Discovery Environment, which is supported by NSF grant number ACI-1548562. The Cosmic Dawn Center is funded by the Danish National Research Foundation.

DATA AVAILABILITY

All the ESO VLT raw spectra used in this paper are publicly available from the ESO archive. The reduced UVES spectra are available in the SQUAD data base (Murphy et al. 2019). The reduced XQ-100 spectra are available from the ESO archive, in the Phase 3 Data Releases section. The lists of fitted absorption lines underlying the obtained results, which are not published in this paper or available from the literature will be shared on reasonable request to the corresponding author.

REFERENCES

Adelberger K. L., Shapley A. E., Steidel C. C., Pettini M., Erb D. K., Reddy N. A., 2005, ApJ, 629, 636
Barai P. et al., 2013, MNRAS, 430, 3213
Becker G. D. et al., 2019, ApJ, 883, 163
Berg T. A. M. et al., 2016, MNRAS, 463, 3021
Berg T. A. M. et al., 2021, MNRAS, 502, 4009
Bergeron J. et al., 2004, The Messenger, 118, 40
Bernstein R. M., Burles S. M., Prochaska J. X., 2015, PASP, 127, 911.
Birnboim Y., Dekel A., 2003, MNRAS, 345, 349
Boksenberg A., Sargent W. L. W, 2015, ApJS, 218, 7
Bordoloi R. et al., 2014, ApJ, 796, 136
Calura F., Matteucci F., 2006, MNRAS, 369, 465
Calura F., Tescari E., D'Odorico V., Viel M., Cristiani S., Kim T.-S., Bolton J. S., 2012, MNRAS, 422, 3019
Carnall A. C. et al., 2015, MNRAS, 451, L16
Carswell R. F., Webb J. K., 2014, Astrophysics Source Code Library, record ascl:1408.015
Cen R., Chisari N. E., 2011, ApJ, 731, 11
Codoreanu A., Ryan-Weber E. V., García L. A., Crighton N. H. M., Becker G. D., Pettini M., Madau P., Venemans B., 2018, MNRAS, 481, 4940
Cooksey K. L., Kao M. M., Simcoe R. A., O'Meara J. M., Prochaska J. X., 2013, ApJ, 763, 37
Cooksey K. L., Prochaska J. X., Thom C., Chen H.-W., 2011, ApJ, 729, 87
Cooksey K. L., Thom C., Prochaska J. X., Chen H.-W., 2010, ApJ, 708, 868
Cooper T. J., Simcoe R. A., Cooksey K. L., Bordoloi R., Miller D. R., Furesz G., Turner M. L., Bañados E., 2019, ApJ, 882, 77
Cowie L. L., Songaila A., Kim T.-S., Hu E. M., 1995, AJ, 109, 1522
Cupani G., D'Odorico V., Cristiani S., Russo S. A., Calderone G., Taffoni G., 2020, Proc. of the SPIE, 11452, 114521U
D'Odorico V. et al., 2013, MNRAS, 435, 1198
D'Odorico V. et al., 2016, MNRAS, 463, 2690
D'Odorico V., Calura F., Cristiani S., Viel M., 2010, MNRAS, 401, 2715
Dalla Vecchia C., Schaye J., 2012, MNRAS, 426, 140
Decarli R. et al., 2018, ApJ, 854, 97
Dekker H., D'Odorico S., Kaufer A., Delabre B., Kotzlowski H., 2000, in Iye M., Moorwood A. F., Proc. SPIE Conf. Ser. Vol. 4008, Optical and IR Telescope Instrumentation and Detectors. SPIE, Bellingham, p. 534
Doughty C., Finlator K., 2019, MNRAS, 489, 2755
Doughty C., Finlator K., Oppenheimer B. D., Davé R., Zackrisson E., 2018, MNRAS, 475, 4717
Ellison S. L., Songaila A., Schaye J., Pettini M., 2000, AJ, 120, 1175
Faucher-Giguère C.-A., Kereš D., Ma C.-P., 2011, MNRAS, 417, 2982
Finlator K., Doughty C., Cai Z., Díaz G., 2020, MNRAS, 493, 3223

Finlator K., Keating L., Oppenheimer B. D., Davé R., Zackrisson E., 2018, MNRAS, 480, 2628
Finlator K., Thompson R., Huang S., Davé R., Zackrisson E., Oppenheimer B. D., 2015, MNRAS, 447, 2526
Fontana A., Ballester P., 1995, The Messenger, 80, 37
Fossati M. et al., 2019, MNRAS, 490, 1451
Fossati M. et al., 2021, MNRAS, 503, 3044
Garcìa L. A., Tescari E., Ryan-Weber E. V., Wyithe J. S. B., 2017, MNRAS, 470, 2494
Haardt F., Madau P., 2001, in Neumann D. M., Van J. T. T., eds, Clusters of galaxies and the high redshift Universe observed in X-rays: recent results of XMM-Newton and Chandra. XXXVIth Rencontres de Moriond
Haardt F., Madau P., 2012, ApJ, 746, 125
Hasan F. et al., 2020, ApJ, 904, 44
Johnson S. D., Chen H.-W., Mulchaey J. S., Schaye J., Straka L. A., 2017, ApJ, 850, L10
Keating L. C., Puchwein E., Haehnelt M. G., Bird S., Bolton J. S., 2016, MNRAS, 461, 606
Kereš D., Katz N., Weinberg D. H., Davé R., 2005, MNRAS, 363, 2
Liang C. J., Chen H-W., 2014, MNRAS, 445, 2061
Lofthouse E. K. et al., 2020, MNRAS, 491, 2057
López S. et al., 2016, A&A, 594, A91
López S. et al., 2018, Nature, 554, 493
López S. et al., 2020, MNRAS, 491, 4442
Madau P., Ferrara A., Rees M. J., 2001, ApJ, 555, 92
Maiolino R., Mannucci F., 2019, A&ARv, 27, 3
Marconi A. et al., 2021, The Messenger, 182, 27
Meyer R. A., Bosman S. E. I., Kakiichi K., Ellis R. S., 2019, MNRAS, 483, 19
Mongardi C., Viel M., D'Odorico V., Kim T.-S., Barai P., Murante G., Monaco P., 2018, MNRAS, 478, 3266
Muratov A. L. et al., 2017, MNRAS, 468, 4170
Murphy M. T., Kacprzak G. G., Savorgnan G. A. D., Carswell R. F., 2019, MNRAS, 482, 3458
Nelson D., Vogelsberger M., Genel S., Sijacki D., Kereš D., Springel V., Hernquist L., 2013, MNRAS, 429, 3353
Oppenheimer B. D., Davé R., 2006, MNRAS, 373, 1265
Oppenheimer B. D., Davé R., Finlator K., 2009, MNRAS, 396, 729
Perrotta S. et al., 2016, MNRAS, 462, 3285
Prochaska J. X., Weiner B., Chen H.-W., Mulchaey J., Cooksey K., 2011, ApJ, 740, 91
Rahmati A., Schaye J., Crain R. A., Oppenheimer B. D., Schaller M., Theuns T., 2016, MNRAS, 459, 310
Reed S. L. et al., 2017, MNRAS, 468, 4702
Rubin K. H. R., Prochaska J. X., Koo D. C., Phillips A. C., 2012, ApJL, 747, L26
Rudie G. C., Steidel C. C., Pettini M., Trainor R. F., Strom A. L., Hummels C. B., Reddy N. A., Shapley A. E., 2019, ApJ, 885, 61
Ryan-Weber E. V., Pettini M., Madau P., Zych B. J., 2009, MNRAS, 395, 1476
Sánchez-Ramírez R. et al., 2016, MNRAS, 456, 4488
Scannapieco E., Pichon C., Aracil B., Petitjean P., Thacker R. J., Pogosyan D., Bergeron J., Couchman H. M. P., 2006, MNRAS, 365, 615
Schaye J., Aguirre A., Kim T-S., Theuns T., Rauch M., Sargent W. L. W., 2003, ApJ, 596, 768
Shull J. M., Danforth C. W., Tilton E. M., 2014, ApJ, 796, 49
Simcoe R. A. et al., 2011, ApJ, 743, 21
Songaila A., 2001, ApJ, 561, L153
Songaila A., 2005, AJ, 130, 1996
Steidel C. C., Erb D. K., Shapley A. E., Pettini M., Reddy N., Bogosavljević M., Rudie G. C., Rakic O., 2010, ApJ, 717, 289
Storrie-Lombardi L., McMahon R. G., Irwin M., 1996, MNRAS, 283, 79
Suresh J., Bird S., Vogelsberger M., Genel S., Torrey P., Sijacki D., Springel V., Hernquist L., 2015, MNRAS, 448, 895
Tescari E., Viel M., D'Odorico V., Cristiani S., Calura F., Borgani S., Tornatore L., 2011, MNRAS, 411, 826
Theuns T., 2021, MNRAS, 500, 2741
Tumlinson J. et al., 2011, Science, 334, 948
Turner M. L., Schaye J., Crain R. A., Theuns T., Wendt M., 2016, MNRAS, 462, 2440
Turner M. L., Schaye J., Steidel C. C., Rudie G. C., Strom A. L., 2014, MNRAS, 445, 794
Tytler D., 1987, ApJ, 321, 49
Tytler D., Fan X.-M., Burles S., Cottrell L., Davis C., Kirkman D., Zuo L., 1995, in Meylan G., ed., QSO Absorption Lines. Springer-Verlag, Berlin, p. 289
van de Voort F., Schaye J., Altay G., Theuns T., 2012, MNRAS, 421, 2809
van de Voort F., Schaye J., Booth C. M., Haas M. R., Dalla Vecchia C., 2011, MNRAS, 414, 2458
Venemans B. P. et al., 2015, ApJ, 801, L11
Werk J. K. et al., 2014, ApJ, 792, 8
Wiersma R. P. C., Schaye J., Theuns T., Dalla Vecchia C., Tornatore L., 2009, MNRAS, 399, 574
Zackrisson E., Inoue A. K., Jensen H., 2013, ApJ, 777, 39

APPENDIX A: UPDATE ON THE $z \sim 6$ C IV ABSORBERS

In this section, we report the lists of C IV lines with $\log N(\mathrm{C\,IV}) \geq 13.0$, used in the present analysis from the three new spectra of quasars at $z \sim 6.5$ (see Section 2.3). A more thorough analysis of all the absorbers detected in those spectra is deferred to a further paper.

Table A1. New C IV absorbers added to the high-z sample.

z_{abs}	b (km s^{-1})	log N(Si IV)
	ATLAS J025.6821−33.4627	
4.78570 ± 0.00006	45 ± 6	13.26 ± 0.03
4.86459 ± 0.00002	23 ± 1	13.15 ± 0.02
4.89616 ± 0.00007[a]	–	13.39 ± 0.02
4.93643 ± 0.00002[a]	–	13.17 ± 0.02
5.18942 ± 0.00004[a]	–	13.43 ± 0.02
5.20948 ± 0.00004	5.0	13.05 ± 0.08
5.21745 ± 0.00007	16 ± 6	13.05 ± 0.07
5.31593 ± 0.00006	46 ± 4	13.67 ± 0.03
5.31795 ± 0.00003	5.0	13.1 ± 0.1
5.31906 ± 0.00007	62 ± 4	13.88 ± 0.03
5.64574 ± 0.00003	6.5	13.2 ± 0.2
5.7354 ± 0.0002	36 ± 13	13.2 ± 0.1
5.76781 ± 0.00009	36 ± 6	13.31 ± 0.05
6.0996 ± 0.0001	39 ± 8	13.34 ± 0.06
	VDES J0224−4711	
4.91166 ± 0.00003	28 ± 4	13.35 ± 0.05
4.9136 ± 0.0001	56 ± 20	13.1 ± 0.1
4.91529 ± 0.00003	19 ± 3	13.25 ± 0.04
4.99276 ± 0.00005	49 ± 5	13.37 ± 0.03
5.00508 ± 0.00003	32 ± 4	14.2 ± 0.1
5.0061 ± 0.0007	58 ± 21	13.7 ± 0.3
5.10894 ± 0.00003	58 ± 2	15.02 ± 0.04
5.11325 ± 0.00003	22 ± 2	14.23 ± 0.05
6.03082 ± 0.00005	16 ± 4	13.62 ± 0.07
6.17255 ± 0.00006	35 ± 4	13.98 ± 0.04
	PSO J036.5078+03.0498	
4.99126 ± 0.00002	51 ± 1	14.39 ± 0.01
5.1488 ± 0.0001	61 ± 7	13.72 ± 0.05
5.2428 ± 0.0001	60 ± 7	13.95 ± 0.04
5.24474 ± 0.00006	22 ± 5	13.58 ± 0.07
5.6885 ± 0.0002	21 ± 13	13.2 ± 0.1
5.8121 ± 0.0001	43 ± 9	13.26 ± 0.07
5.8262 ± 0.0001	50 ± 8.	13.44 ± 0.05
5.89869 ± 0.00004	9 ± 4	13.7 ± 0.1
5.90223 ± 0.00001	32 ± 8	13.2 ± 0.1

Notes. [a] Combination of two lines closer than $\Delta v = 50$ km s^{-1}. See Section 2.1.

This paper has been typeset from a TEX/LATEX file prepared by the author.